Development and Flight Validation of an Autonomous Mono-Wing UAS

Kingsley Fregene, Steve Jameson, David Sharp

Lockheed Martin Advanced Technology Laboratories
Cherry Hill, NJ 08002
{kingsley.fregene, stephen.m.jameson, david.sharp}@lmco.com

Harold Youngren

AeroCraft Consulting
Portland, ME 04103
guppy@maine.rr.com

David Stuart

Dave Stuart Model Aircraft,
Clarkston, UT 84304
jupiter-dls@comcast.net

ABSTRACT

This paper describes the development and flight validation of the Samarai Demonstrator Air Vehicle (DAV). The DAV is a fully autonomous rotating single-wing unmanned aerial system (UAS) with vertical takeoff and landing (VTOL) capability, full authority flight controls and rotating frame sensing, and guidance and navigation. It was developed as a demonstrator for a nano-class UAS at Lockheed Martin Advanced Technology Laboratories (LM ATL).

NOTATION

A	=	disk area
C_D	=	drag coefficient
CT	=	thrust coefficient = $T/\rho A(\Omega R)^2$
FM	=	figure of merit = P_{ideal}/P
		where $P_{ideal} = T\sqrt{\frac{T}{2\rho A}}$
J	=	propeller advance ratio = $V_{prop}/n2\pi R_{prop}$
R,R_{prop}	=	Rotor tip radius, propeller radius
V	=	forward velocity
α	=	disk angle of attack
κ_i	=	rotor induced power factor
ρ	=	air density
σ	=	rotor solidity = $c/\pi R$
μ	=	tip speed ratio = $V\cos\alpha/\Omega R$
ν	=	rotor induced velocity

INTRODUCTION

Recent interest in developing smaller micro air vehicles (MAVs) capable of indoor and outdoor operation has resulted in various designs that offer hover and VTOL. To achieve designs at the micro scale for indoor and outdoor flight, there has been an increased focus on biologically-inspired air vehicles. These vehicles are conceptualized from flyers and gliders found in the natural world, including flapping wing designs motivated by insect or bird flight [1] and single-winged flyers inspired by fruits and seeds (or *samaras*) [2, 3]. Other MAVs use small-scale conventional designs based on rotorcraft forms including standard helicopters, dual coaxial rotor-copters [4] and quad rotor copters [5].

In this paper, we describe the Samarai Demonstrator Air Vehicle (DAV) shown in Figure 1. It is a demonstrator vehicle for the nano scale *Samarai* air vehicle shown in Figure 2 and described in [2]. We describe a complete air vehicle development process including modeling and simulation, guidance and control, flight experiments, and validation of simulation models. Unlike the flapping wing and helicopter-based designs, a rotating single-wing vehicle is inherently stable in hover, mechanically simple and robust. It also has clean aerodynamics and few moving parts. It is biomimetic, but its operation does not depend on fragile feathers, delicate wings or precision moving parts. Controlling the DAV is also easier because of the vehicle's dynamic stability and the absence of a fuselage. Control is simplified to controlling a virtual disk created by the spinning blade. The motion of the disk is similar to, but simpler than, a helicopter or flapping wing vehicle. Because, for a given dimensional constraint, the greatest Reynolds

Figure 1. Samarai Demonstrator Air Vehicle just prior to takeoff in an outdoor flight environment. The vehicle takes off vertically from a launch pin in the ground and lands vertically on the avionics pod cover.

Presented at the American Helicopter Society 66th Annual Forum, Phoenix, Arizona, May 11-13, 2010.

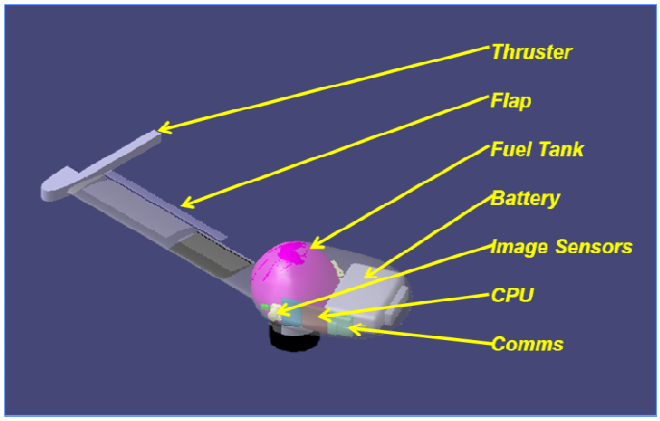

Figure 2. Samarai Nano Air Vehicle Design is the ultimate target for which the DAV was developed as a demonstrator. Unlike the DAV, it is propelled by a tip-jet; has both the propulsion and control actuation systems on the same side of the central hub and is approximately 10x smaller than the demonstrator.

number for a flight vehicle is achievable with a rotating wing, a samara-like configuration can have a wing loading one tenth that of a conventional helicopter or flapping wing design of the same size. The lower loading greatly reduces the power requirement for a given endurance. Indeed, it was shown recently that a single rotating wing requires half as much power as a flapping wing to achieve a comparable level of flight performance [6]. In addition to these airframe-specific advantages, there are numerous practical advantages that the Samarai monocopter presents for a usable small air vehicle. One advantage is portability, as it might be carried by a soldier or first responder for information gathering. The Samarai DAV provides VTOL and hover capabilities similar to a helicopter, but with greatly reduced mechanical complexity. The DAV essentially has two moving parts – a motor/propeller and an actuator/flap assembly. This simple design results in much greater reliability and robustness in harsh operating environments (as compared with a traditional helicopter of similar size). In addition, the DAV is a single linear body, enabling compact storage and transport that does not require disassembly and reassembly. The mechanical simplicity reduces the weight required for components that do not produce thrust or lift, enabling a greater payload fraction or equally longer endurance for a given payload. Finally, the simple design results in a significantly reduced production cost. The prototypes described in this paper cost approximately $500 each for parts and materials, which also greatly reduce repair and maintenance costs.

Previous work by Lockheed Martin, including that described in [2], has done extensive design, analysis, and experimentation to validate the potential of the Samarai as a design concept for micro-scale air vehicles (Figure 2).

The vehicles described in this paper have a wing span of approximately 76 cm, and weigh approximately 600 g when fully equipped. Using these vehicles, we were able to demonstrate indoor and outdoor flight, in operator controlled mode using standard radio control handsets, and in fully autonomous flight using both GPS-guided and non-GPS guided flight modes. All processing for sensing, control, and autonomous guidance was performed using a pair of on board processors.

Other researchers have done similar work with single-wing or mono-copter designs, including [3, 7-10], but none has reported detailed control design and flight-validated vehicle modeling in multiple degrees of freedom as described in this paper. Also, to the best of our knowledge, no other work has demonstrated fully autonomous flight with onboard sensing, guidance and control.

AIR VEHICLE DESIGN

The design of the Samarai DAV is derived from the free-flight monocopters of Charles W. McCutchen [11]. The DAV's general configuration is similar to McCutchen's vehicle, with a single blade opposing a boom. A motor driving a small propeller is mounted on the boom to provide propulsion. It uses a weighted balance boom mounted orthogonally to the blade/motor boom. This boom allows the vehicle to balance and provides gyroscopic stability. The DAV differs from McCutchen's designs in that a movable control surface is hinged directly to the trailing edge of the outer half of the rotor blade (instead of a stabilizer mounted on vertical struts). A vertical fin is also employed at the tip of DAV's rotor to enhance stability. The mass balance boom is inclined downward, inducing a positive angle of attack to the blade as the vehicle rotates. The center of gravity is located near the root end of the blade, and is co-located with a payload pod bonded to the underside of the blade. A servo, mounted at the root end of the blade, drives the control surface (an aerodynamic flap) through a torque tube. An electric motor and propeller are mounted in a tractor configuration to the motor boom providing propulsion. The design is shown in Figure 3.

Early calculations, aimed at sizing the vehicle, showed that a vehicle with a rotor semi-span of 83.8 cm and a chord of 7.62 cm would provide sufficient lift for the vehicle, plus a 150 g payload with some margin left for subsequent increases in weight. An initial gross weight of about 595 g was predicted. It was determined that an electric power system with approximately 130 Watts (100 Watts/pound GTOW) of input power would be adequate to power the vehicle. The vehicle characteristics are summarized in Table 1.

The rotor blade is constructed of balsa wood of approximately 112 kg/m^3 density shaped with an airfoil

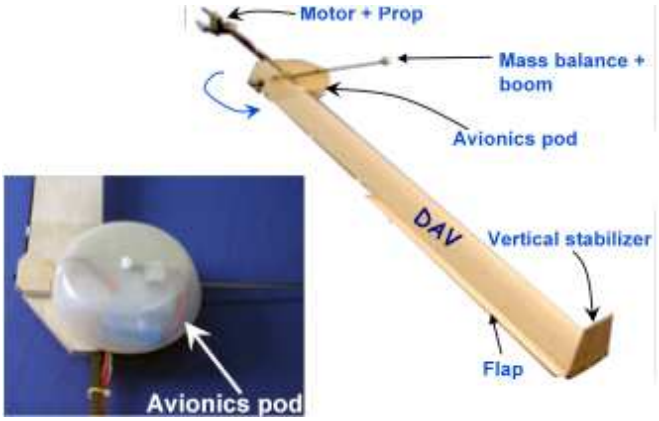

Figure 3. Design elements of the Samarai DAV. The motor/prop combination provides propulsion, a trailing edge flap controls vehicle motion, the mass balance/boom and vertical stabilizer contribute to flight stability. The avionics pod contains sensors, electronics and computational unit for overall vehicle operation.

Table 1. DAV flight vehicle characteristics

Wing radius	76cm
GTOW	600g
Speed	7 m/s
Payload	300g
Endurance	10 mins.
Rotation Rate	300 RPM

cross-section similar to a thinned (8.3%) Clark Y. For increased durability and moisture proofing, the blade is covered with silkspan (fiber reinforced paper) saturated with a water-borne polyurethane varnish. A 2.4 mm thick balsa control surface 25.4 mm wide and 406 mm long is hinged tothe outer half of the blade at its trailing edge. A servo is mounted at the root end of the blade, and drives the control surface through a 3 mm carbon fiber torque-tube installed along the blade trailing edge. At the tip of the blade, a 2.4 mm thick balsa vertical stabilizer is installed with nylon screws to allow for easy removal or replacement. Opposite the blade, an 8 mm square-tube motor-boom is bonded to the blade root. This tube is filled with a micro-balloon/epoxy resin mixture to increase its resistance to breakage and is wrapped externally with heavy cotton thread and glue to reduce delamination. The electric motor and propeller are attached to the motor-boom with a clamp to facilitate balance changes.

The payload/avionics pod shown in Figure 3 is bonded to the underside of the blade root and houses the payload, motor battery, electronic speed control and radio control receiver. The base plate is made of balsa, reinforced with fiberglass and the bowl-shaped cover is made of molded fiberglass. The cover is attached to the base plate with a single nylon screw and nut. The screw is also located at the vehicle's center of gravity / rotation and is drilled through lengthwise to accept the launching pin. The balance boom is made from a 4.76 mm carbon tube with a lead weight screwed to the outboard end. The balance boom is attached to the top of the base plate using a clamp for ease of adjustment. The DAV propulsion system uses a brushless, 2800 Kv, in-runner electric motor driving a 15 cm diameter propeller; a 2 cell, 2.1 amp-hour lithium polymer motor battery and an 18 amp electronic speed control. The speed control also provides 6 V power for the avionics and servo.

Vehicle Performance and Flight Power

The performance of the DAV was estimated using helicopter performance methodology based on a momentum theory model for induced power, a profile power model for rotor drag and a parasite power model for forward flight power [12, 13].

$$P = T\left[V\sin\alpha + \kappa_i v + \frac{C_{d0}(\Omega R)}{8\left(C_T/\sigma\right)}(1+4.5\mu^2+1.61\mu^{3.7})f(\alpha)\right]$$

The rotor power uses an induced power factor k_i that scales the ideal induced power and a profile drag contribution scaled by functions of the advance ratio and disk angle. Here f(a) is defined as

$$f(\alpha) = 1-[0.03+0.10\mu+0.05\sin(4.304\mu-0.20)](1-\cos^2\alpha)$$

The induced velocity (v) in the expression for power is the downwash velocity at the disk and is defined by inflow velocity and the hover downwash velocity

$$v = \frac{{v_h}^2}{\sqrt{(V\cos\alpha)^2+(V\sin\alpha+v)^2}} \text{ with } v_h = \sqrt{\frac{T}{2\rho A}}$$

Parasite power was determined using drag areas for all non-rotor components in forward flight, balancing drag with tilting of the thrust vector by the disk angle. Additional torques due to motor, boom, and rudder drag were included as additional contributions to overall torque. This momentum model was tuned by measurements of electric power from flight-testing and wind tunnel tests of the propeller and motor efficiency. This data was used to set the induced power factor and average blade section drag. Using this approach, Figure 4 shows the flight power and power breakdown (induced, profile and parasite) from the DAV analytical model as a function of flight speed. Note that this plot shows the mechanical power delivered to the airframe from the propeller, not the electrical power required for flight (which is quite a bit higher, given the efficiency of the propulsion system described in more detail in the following section on Flight Testing). Note that the measured top-speed of the vehicle during flight test closely matched the minimum power speed of 6-7 m/s in Figure 4.

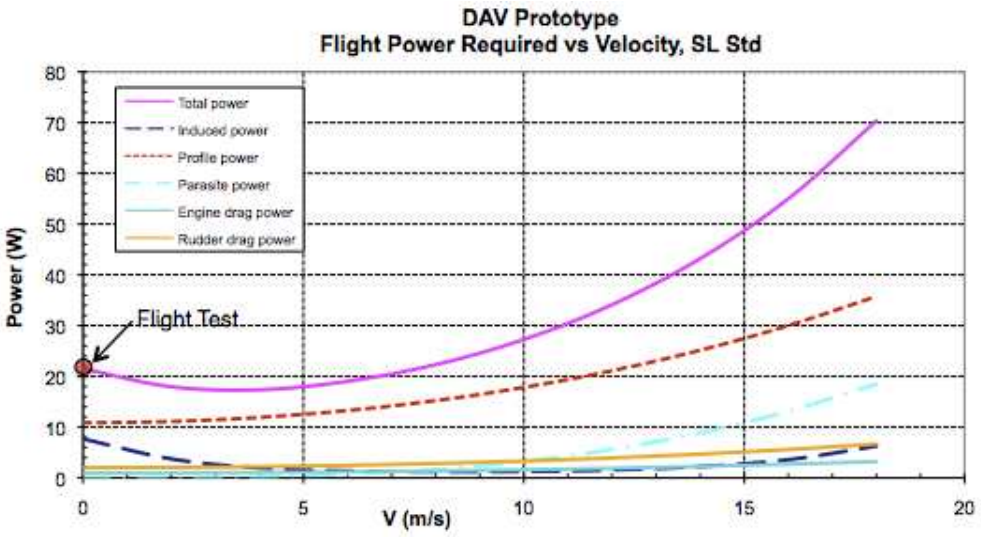

Figure 4. Flight power breakdown for the DAV using modified momentum theory analysis

Vehicle Control System Architecture

The overall closed loop control system that includes the DAV is shown in Figure 5. External commands or onboard mission profiles are converted to guidance commands that drive a control law to generate control commands to the vehicle. Onboard sensors measure the state of the vehicle and a state estimator fuses these into state variables that are fed back to the guidance and control system. These components will be described in the sections that follow.

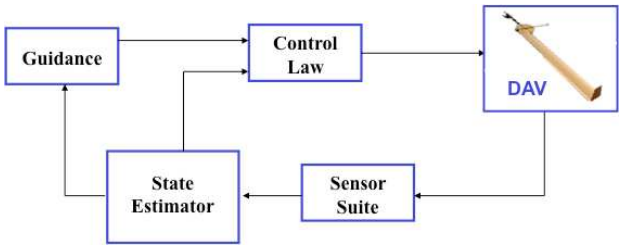

Figure 5. Block diagram of overall closed loop system for the Samarai DAV

VEHICLE MODELING

An empirical model is developed for use in state estimation and for performing simulations. The model shown in Figure 6 maps flap and throttle control inputs through empirical models of the actuators to climb/descent rates and translational velocities with simplifying assumptions on aerodynamic loading.

To create the vehicle model, flight test data was collected for several combinations of throttle setting (matched to overall vehicle rotation rates) and collective/cyclic flap commands and corresponding climb rates and forward speed measured by on-board sensors. Flight data was then put in a set of two dimensional table lookups with constraints that are indicative of actual vehicle parameters. Separate flight data were collected for vertical and lateral motion, resulting in the manifolds shown in Figures 7(a) and 7(b).

Figure 7(a) shows that, in general, negative values of collective flap (flap down) generally resulted in positive

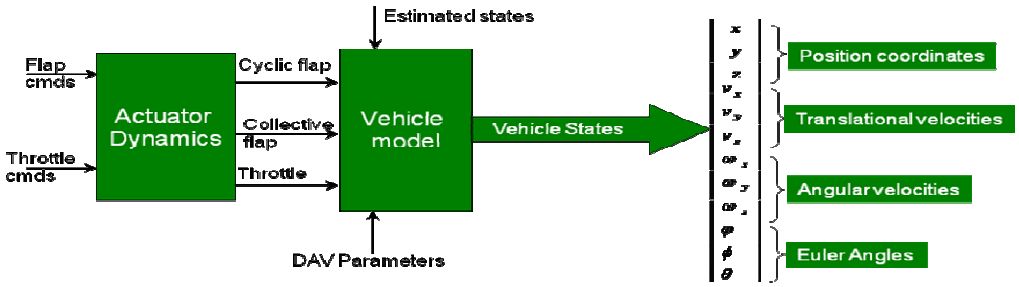

Figure 6. The empirical modeling approach uses experimental data to model the flap actuator and throttle dynamics as well as flight test data that represents mapping from vehicle rotation rate and cyclic/collective flap to forward flight speed and climb rate.

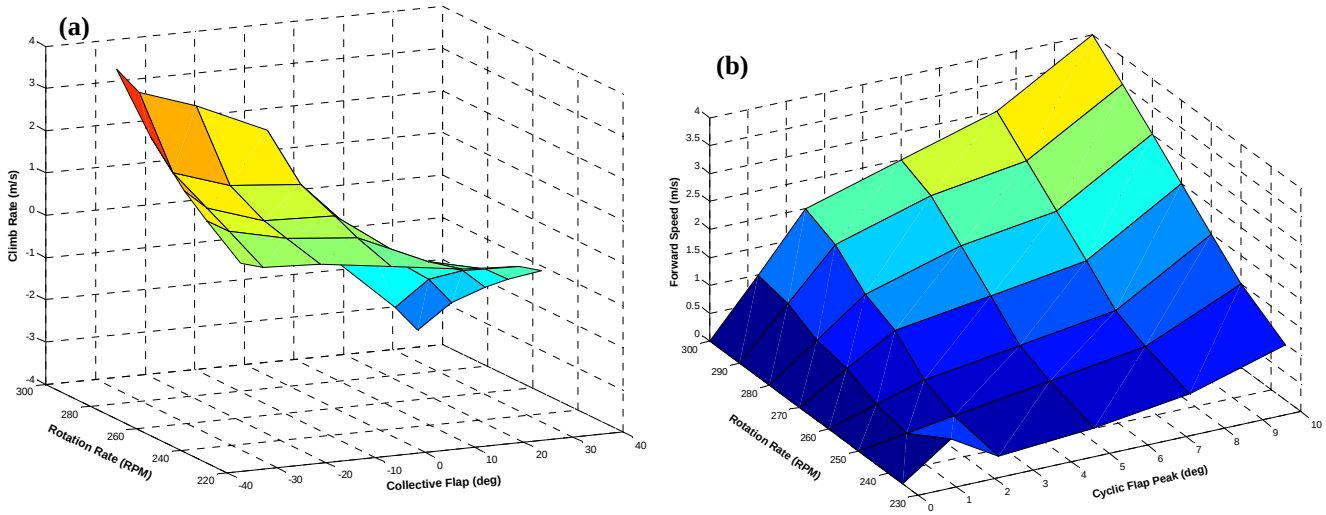

Figure 7. Vertical flight manifold (a) depicts the relationship between the collective flap/rotation rate and climb rate. Lateral flight manifold (b) shows how the forward speed evolves with rotation rate and cyclic flap peaks.

climb rates. However, it is evident that, as the vehicle's rotation rate decreased, climb rates were negative because insufficient lift was being generated to keep the vehicle airborne. Apart from an anomaly at cyclic flap magnitude = 1 deg (most likely an erroneous sensor measurement) in Figure 7(b), increases in cyclic flap magnitude and rotation rate resulted in higher forward flight speeds.

The flap actuator model was also created from empirical data of servo response to commanded deflections, resulting in a cascade of two second order transfer functions parameterized by a pair of natural frequency and damping terms. The throttle response was modeled as a first order transfer function based on empirical data.

Model Validation

To validate this model, a closed loop simulation that incorporates guidance and control components is created in MATLAB/Simulink. Specific flight experiments were then run and state data logged. The same experimental scenarios were repeated purely in simulation using the developed empirical model. The results showed good agreement between the empirical model and experimental data (look ahead to Results section for details).

AVIONICS AND VEHICLE STATE ESTIMATION

Sensors in the avionics suite for the DAV are shown in Figure 8. These include a magnetometer (to sense rotational phase and determine spin rate), a barometric altimeter (to measure height and allow estimation of climb rate), a pair of thermopiles (to measure disk tilt and allow estimation of attitude rates) and a GPS (for position and velocity measurement). All of these are processed on an onboard flight computer running an Extended Kalman Filter to provide estimates of state variables required for control law synthesis.

Sensor	State Component Sensed
Thermopile	Disk Tilt (from differential), Attitude Rate
2-axis Magnetometer	Disk Yaw, Spin Rate
Barometer	Altitude, Climb Rate
GPS	Position, Velocity

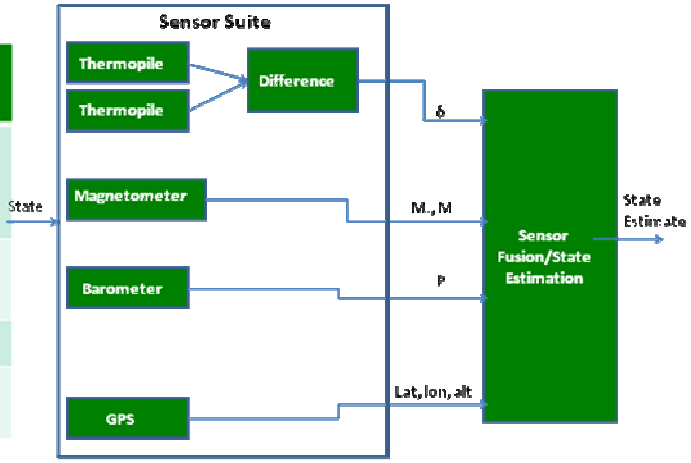

Figure 8. The DAV avionics package contains a suite of sensors designed to measure and/or estimate all the states needed for full-authority vehicle control.

This flight computer is where all sensor processing, state estimation and control algorithms are run. It is a gumstix single board computer identified as *Main Processor* in Figure 9, which shows the actual avionics hardware with all sensors and computing resources.

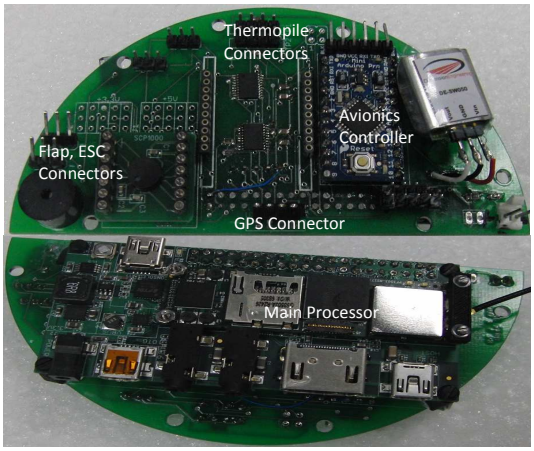

Figure 9. DAV avionics board showing key components like the main processor and the avionics controller (an embedded micro-controller that drives the actuators).

Vehicle flap deflections and throttle setting are carried out using an embedded micro-controller that receives desired values for these from the gumstix computer. State estimation and control laws implemented in MATLAB/SIMULINK and used in end-to-end simulation are autocoded and downloaded to the gumstix computer for actual flight experimentation.

VEHICLE STATE ESTIMATION

State Estimation is accomplished by using a set of filters that when combined provide a single estimate of the state. The state of the vehicle at any time *t* corresponds to the states of the empirical vehicle model described in Figure 6. It is a 12-element vector defined as follows:

$$s_t = \begin{bmatrix} x_t & y_t & z_t & v_{x_t} & v_{y_t} & v_{z_t} & \omega_{x_t} & \omega_{y_t} & \omega_{z_t} & \psi_t & \phi_t & \theta_t \end{bmatrix}$$

where [*x*, *y*, *z*] correspond to the position of the vehicle, [v_x, v_y ,v_z] describe the translational velocities of the vehicle, [ω_x, ω_y, ω_z] describe the rotational velocities and [ψ,ϕ, θ] describe the yaw, roll and pitch of the vehicle.

Raw sensors are generally pre-processed in some form before being used in the state estimation scheme. For instance, raw magnetometer data is passed through a FIR-filter in order to reduce noise. Rotational phase (ψ) and rotation rate (ω_x) are then computed and added to a vector of sensor measurements for use in later steps of the state estimation.

The primary filter used in the estimation is the Extended Kalman Filter (EKF), which behaves similarly to a Kalman Filter but allows for nonlinear state transitions. The EKF estimates state by representing the state of the vehicle as a mean, μ, and covariance, Σ, and tracking these two parameters over time. State estimation is accomplished in two phases: prediction and measurement. The prediction phase propagates the state from the previous time step by using the control commands sent to the vehicle and a model of how the vehicle responds to control commands. In other words, it predicts the current states of the vehicle by using its knowledge of the previous states and assumptions about how the vehicle should have moved during the previous time step. (The prediction model used in this phase is the empirical model described earlier Figure 6). The second phase refines the prediction made in the first phase by considering sensor measurements.

GUIDANCE AND CONTROL

The main control problem solved for the DAV can be stated as follows: "How can a wholly rotating single-wing UAV maintain lift and also control its translation to specified points?" In a conventional helicopter, this problem would be solved by adjusting the angles of the rotor blade in flight using a swashplate to change the direction of thrust generated from the blade. Although rotating mono-wing aircrafts are similar to helicopters in some sense, actively controlling the blade angle is infeasible due to the sensing, processing and actuation requirements it would entail. Our solution to this problem is to create a "virtual swashplate" that consists of the entire rotor disk controlled using a single flap. In this scheme, flap deflections are modulated at precise rotational phase angles to generate forces/moments needed to sustain lift and also tilt the rotor disk by an appropriate amount in the desired direction of flight—all without the use of a physical swashplate mechanism. This is illustrated in Figure 10.

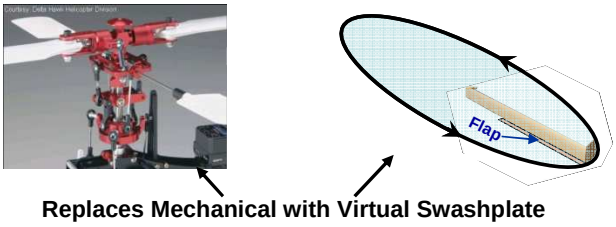

Figure 10. The control approach for DAV essentially replaces a mechanical swashplate with a virtual one.

The overall implementation of an autonomous guidance and control system using the virtual swashplate is shown in Figure 11. It is designed in a simplified outer-inner loop manner, with the virtual swashplate (the flap control system in Figure 11) at the core of the inner loop while the velocity

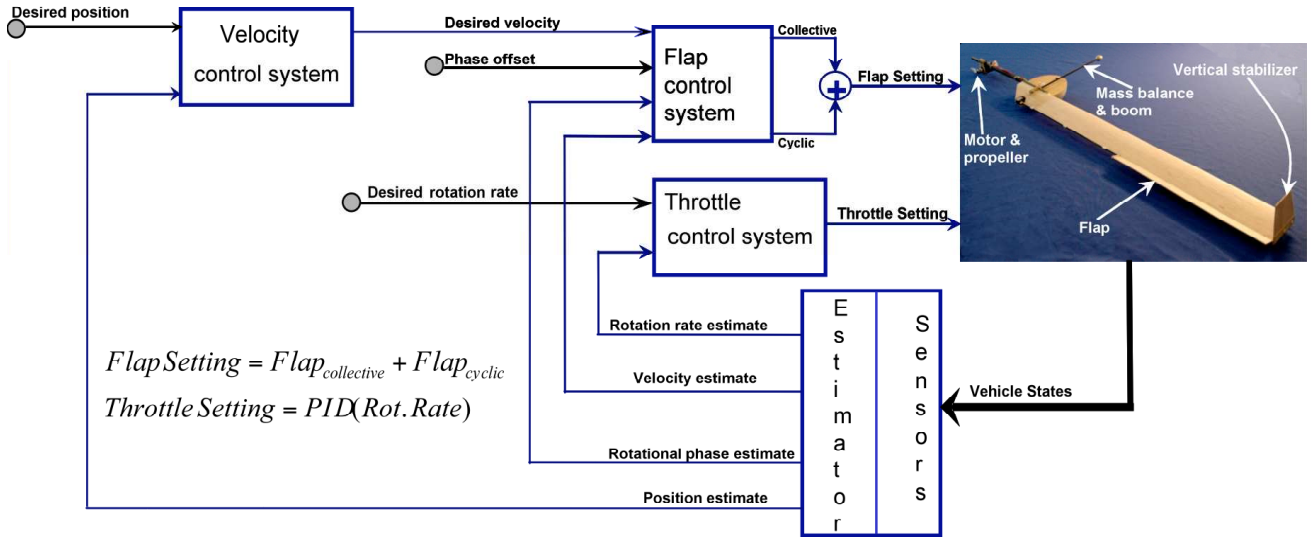

Figure 11. DAV guidance and control methodology.

control system makes up the outer loop. This enables the vehicle to be operable in multiple modes. In *joystick mode*, an operator controls throttle, collective and cyclic from a joystick with the aid of a simple avionics package. The avionics package translates operator desired heading into virtual swashplate commands using vehicle rotational phase measured by a magnetometer. In this mode, only a portion of the flap control system is active. In *velocity mode*, missions are specified by desired speed, heading, and duration for each flight segment (bypassing the velocity control module). Therefore, the flap control system uses velocity feedback and desired phase offset to calculate flap commands that enable the vehicle track the desired speed and heading commands. In *waypoint mode*, missions are specified as waypoints in three dimensions using GPS coordinates (outdoors) or relative position coordinates (indoors). The velocity control system converts the waypoint commands into desired velocities for each motion segment. These are then propagated down the feedback control loops in the same manner as the velocity mode except that the commanded speed and heading information are embedded in the desired velocity command automatically computed by the outer loop.

Consequently, the controller generates appropriate flap and throttle commands to achieve the desired waypoint. Position commands are converted into desired velocities that are subsequently mapped to specific collective and/or cyclic flap deflections, depending on whether commanded motion is mostly in the vertical or translational plane. Collective flap inputs are generated in response to ascent / descent / hover commands while cyclic flap inputs are generated in response to translational motion commands and hover commands (to counter the effect of side forces). Engine throttle or desired thrust setting is computed indirectly by controlling the rotation rate of the vehicle using a PID-type controller.

RESULTS

The DAV was successfully flown in many flight trials in both indoor and outdoor environments. Flight-testing activities included vehicle flight power and propulsion tests and controls development and testing. Vehicle control was successfully demonstrated in both simulation and flight experiments. Capabilities demonstrated include autonomous control of overall vehicle rotation rate, take-off and landing, height control, hover control and translation to commanded waypoints.

Flight Power Measurements

Flight testing for the DAV included propulsion testing for calibration and validation of performance models. This was done by measuring the propulsion electrical power with an on-board data recorder. An EagleTree eLogger (~20 g) was used to record the power delivered from the battery to the onboard avionics and propulsion system. For this work, the vehicle was flown in short series of flights that consisted of an initial climb out of ground-effect followed by a stable hover where power and altitude were held constant to obtain power measurements. Power (volts and current) from the battery was logged as a function of time as shown in Figure 12. Propeller RPM was also measured in some flights. In this test power levels of roughly 74 W were recorded for hover out-of-ground-effect for several flights. The base power level of 2 W was established for the avionics, giving a net electrical hover power of 72 W. One of the flights in this group showed a somewhat lower power level of 62 W but this power level was not repeatable.

Flight power tests such as these show the total power required for flight but do not (by themselves) establish the rotor power levels required for hover. The missing component is the efficiency of the propeller and electric

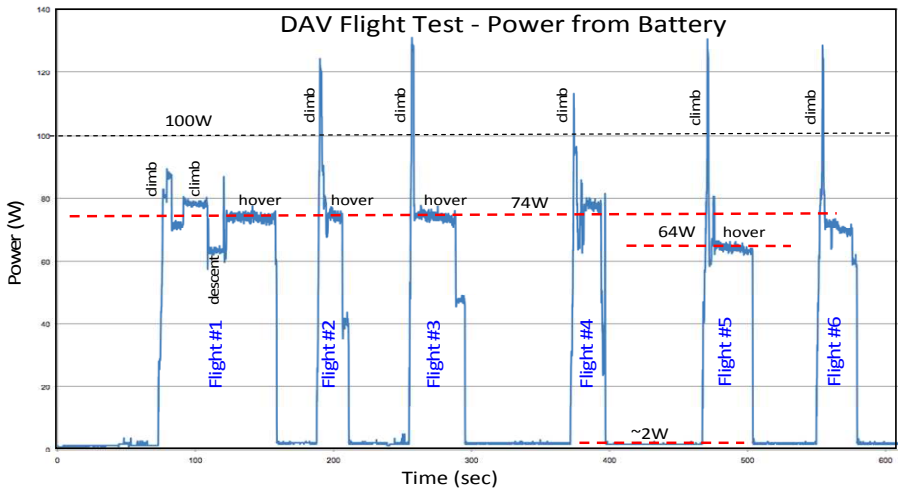

Figure 12. DAV flight test power measurements for hover out-of-ground-effect showing overall electrical flight power of 72 W.

motor that deliver torque to the rotor itself. In order to determine rotor power additional testing was done for the propeller/motor/controller as a propulsion system component. This was done by mounting the motor and propeller from the DAV in the MIT Low Speed Wind Tunnel to measure thrust, torque, RPM and electrical input power as a function of inflow velocity to the propeller. The DAV uses a motor and propeller mounted in a tractor configuration at 40% of the rotor radius which gives a typical inflow speed at 300 RPM of 11 m/s. Test results for overall propulsion efficiency (defined as $T_{prop}V_{prop}/P_{in}$)at inflow velocities of 5, 10 and 15 m/s are shown in Figure 13, plotted as a function of propeller advance ratio J.

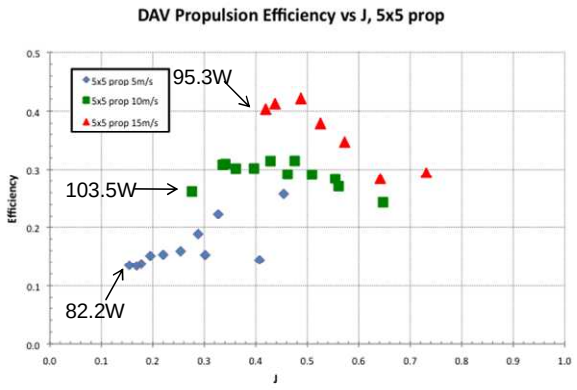

Figure 13. Measurements of DAV propulsion system efficiency (propeller, motor, and controller) as a function of advance ratio and inflow velocity from MIT wind tunnel.

This data shows that peak power levels at full throttle range from 82 to 103 W at low advance ratios (high RPM) and that combined propulsive efficiencies of ~30% are typical for operation at 10 m/s inflow. Measurements of torque were noisier than overall power but indicated that motor efficiency was roughly 75% and propeller efficiency was 40% at this operating point. Note that overall propulsion efficiency increases to slightly more than 40% at 15 m/s. These are unexpectedly low propulsion efficiencies and help explain why power levels of 70 W or more are required to fly this rotor. The reduced propulsive efficiency may be due to low Reynolds numbers on these small propellers and the low inflow speeds that represent near-static conditions for propeller operation. Operation of these propellers at higher inflow speeds would substantially increase overall propulsion efficiency for this vehicle.

The modified momentum theory model discussed previously was calibrated using a propulsion system efficiency of 32% (corresponding to 11 m/s speed at the DAV propeller) using the measured flight power of 72 W. The power levels from the momentum model were tuned to this total flight power (with a net rotor hover power of 23 W) using an induced factor of k_i = 1.5 and an average rotor C_d = 0.043. These values were used to produce the flight power estimates in Figure 4. Note that this data gives a rotor hover figure of merit (FM) of 0.26 (corresponding to the 23 W of rotor power). The overall electrical power required for flight at sea level conditions as a function of velocity is shown in Figure 14.

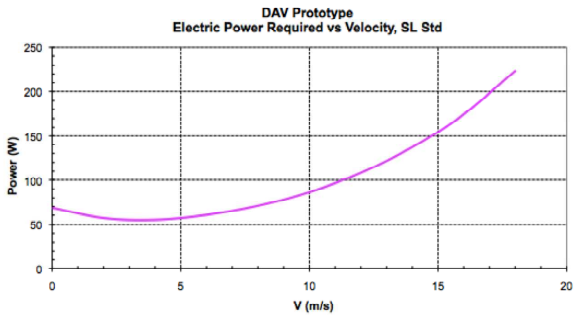

Figure 14. Overall electrical power required for DAV propulsion vs. velocity

Outdoor Flight Control Experiments

To perform flight control experiments with the DAV, an ad-hoc wireless network is set up directly at the test facility, with the vehicle as one node in an ensemble that includes an operator console unit (essentially, a laptop) to upload mission waypoints and receive telemetry downlink. Once the mission is initiated, the DAV takes off autonomously, executes the various mission segments and lands autonomously.

A flight test done at Lakehurst Naval Air Station (Lakehurst, NJ) in the presence of winds blowing in a south-easterly direction is typical of performance observed in experiments. In this experiment, the vehicle is commanded to takeoff and hover autonomously at a height of 10.0 m above the launch point. Data from the flight experiment are shown in Figure 15. The figure on the right-hand side shows the flight path while the figure on the left depicts time-stamped vehicle height and position trajectories (North and East of the launch point).

The flight segments identified by letters (a) – (d) can be described as follows:

a) Shows that the vehicle drifts eastward on takeoff.
b) Shows that wind blows the vehicle in a south-easterly direction.
c) The DAV hovers at a height of 10m (as commanded), but south east of the launch point. Note that the flat lines on the East and North trajectory suggest GPS dropout, rather than position hold from time t=13 s to t=58 s.
d) In this segment, the vehicle is retrieved and returned by the operator.

Indoor Flight Experiments

A representative autonomous indoor flight scenario is as follows:

- Ascend to 3.0 m above ground level, hover.
- Fly to a point 43 m North and 18 m West of the launch point, hover.
- Return to launch point, hover.
- Land.

Flight test results are shown in Figure 16.

As was observed in the outdoor experiment, the flight path result shows a slight east-ward drift on takeoff (motion in the other coordinate is North in this case). A comparison of the height response in Figures 15 and 16 show that height control performance during indoor flight is inferior to what was observed outdoors. This is likely due to the fact that operating outdoors enabled higher commanded heights (in this case 10 m) than indoors. The precision of the height sensor was within the commanded height (3 m) for indoor flight, leading to poor altitude hold. Furthermore, indoor pressure fluctuations have an impact on sensed pressure, which is what the barometric altimeter sensor measurements is based on. As can be seen from the approximate periodicity of the height measurements on Figure 16 (lower right hand corner), wind oscillations outdoors caused a corresponding pressure oscillation in the indoor tent-like space that the barometric altimeter picked up. This effect was not observed in outdoor flights using the exact same height control system (see Figure 15 top-left). On the average, the experimental data shows that the vehicle overshoots the commanded height by 1.0 m. Note that the height data shown on Figure 16 (lower right hand corner) represents raw sensor data.

The effect of GPS lag on vehicle flight path is that rectilinear navigation to waypoints was not achieved. For instance, to fly from the launch point to the goal, desired heading angle. should be around 112 degrees (using a Cartesian frame that increases counter-clockwise from East). Ideally, peaks of the

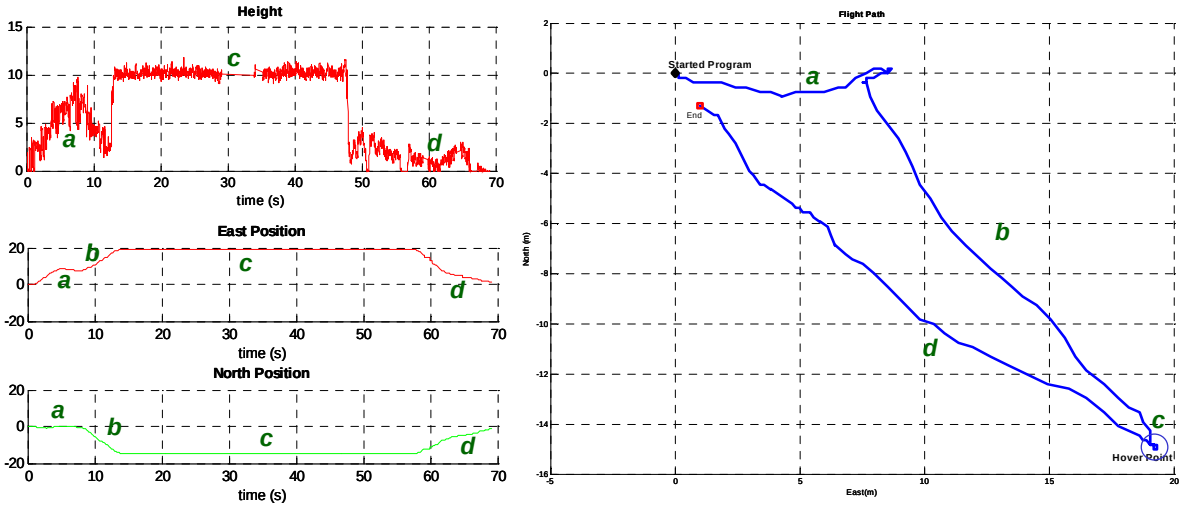

Figure 15. DAV outdoor flight experiment results show very good altitude hold performance, but some susceptibility to wind effect.

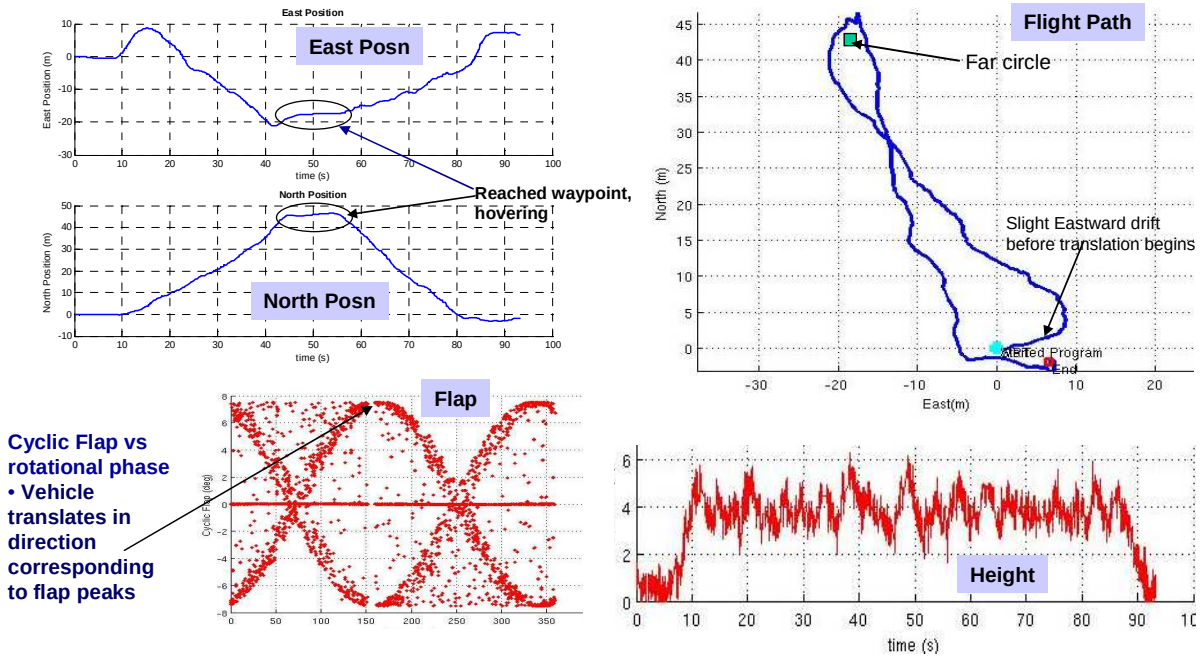

Figure 16. Indoor flight experiment results show that the DAV attains all way points (see flight path on top right and trajectory on top left); maintains commanded height to within 1m and cyclic flap phase that match desired heading for flight from origin to goal point and return.

cyclic flap deflection should occur when the vehicle's rotational phase equals this desired heading. However, the impact of computation delays, flap actuator dynamics and the DAV's rotational dynamics introduced a phase shift of ~ 30 degrees as seen in the flap response of Figure 16.

Validation of Simulation Results

To validate the modeling and simulation approach, the indoor scenario was run through a closed loop simulation of the empirical model using the same guidance and control and estimator as used in the flight experiments. The modeling/simulation results were compared with data from flight experiments and ideal DAV response (the response that would be obtained if the guidance and control technique resulted in perfect closed loop response). Figure 17 shows flight-path and trajectories of the indoor flight scenario.

The flight data lags ideal response by ~8 s while the simulation lags empirical data by ~5 s. The simulation also overshoots the ideal response and flight data by ~5 m. In spite of GPS induced lags in position update, the path from

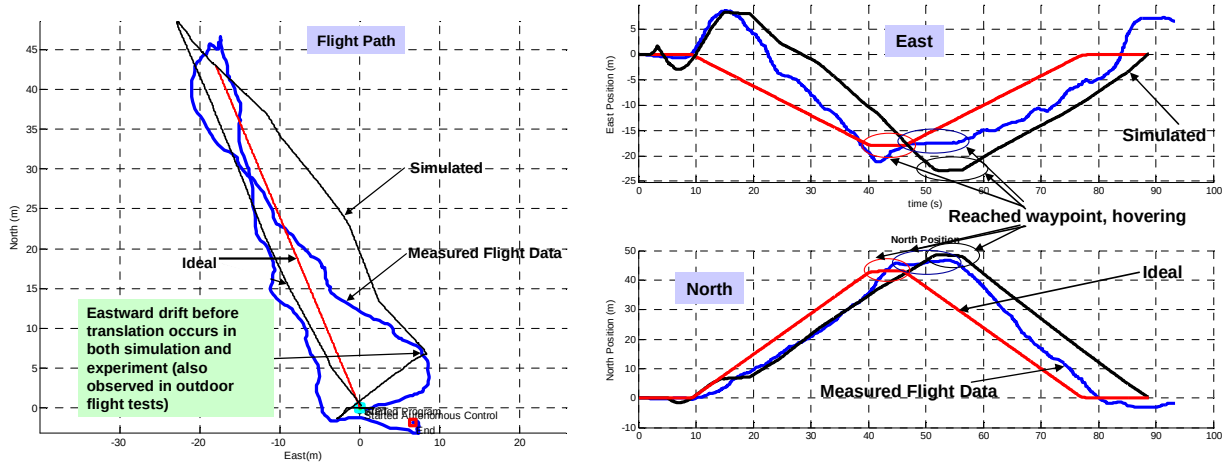

Figure 17. Flight path (left) and position trajectories (right) from flight experiments, simulation and ideal response. Because the guidance approach was waypoint-to-waypoint rather than constrained guidance along the ideal path, the control objective was to attain the waypoint, not strictly follow the ideal path.

flight data compares favorably with ideal rectilinear path and flight path from simulation. Figure 18 compares the altitude hold performance and ability to control overall vehicle rotation rate.

Figure 19 shows the cyclic flap deflection over time during this mission. In simulation, there is cyclic flapping to counter the tendency to drift sideways on take-off (from t=0 to 9 s), which is not evident in the ideal response or experimental data. The fact that the simulation also takes longer than both the ideal and flight data to reach the waypoint is seen in that cyclic flap returns to zero at t=40 s for ideal, t=42 s for flight experiment and t=47 s for the simulation. The simulation tends to require slight cyclic flapping to maintain hover.

CONCLUSIONS

Our previous work has shown the potential for the Samarai concept as a design for micro-scale air vehicles. The work described in this paper has made that potential a reality, with

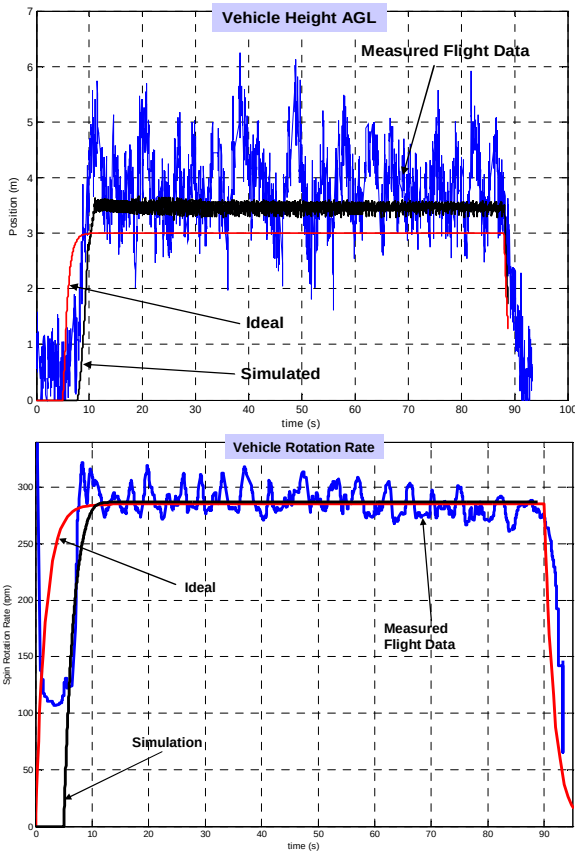

Figure 18. DAV altitude hold response (top) and overall rotation rate control (bottom) showing that simulation tracks command to ~0.5m and flight data to within 1m (average). The vehicle rotation rate is held to within ~10 RPM of commanded, while simulation tracks command to within 3RPM.

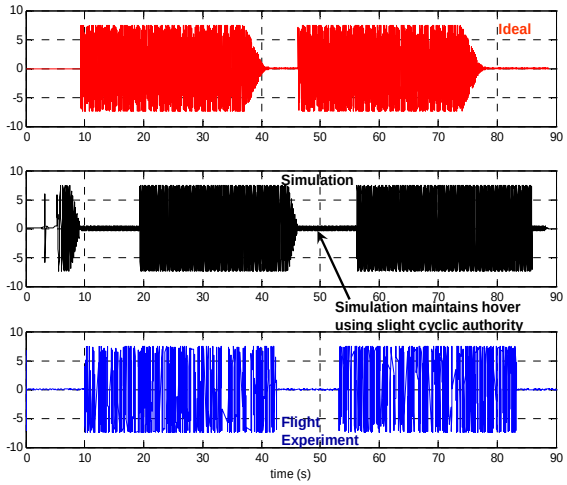

Figure 19. Cyclic flap deflection over time shows the same level of cyclic flap peaks for simulation, ideal and flight test performance. In all cases, cyclic flap peak drops to almost zero for hovering at the second waypoint, other than in simulation where a slight cyclic flap was needed to hold station.

demonstrations of fully autonomous flight, controlled by an onboard sensing and processing suite. Through this work, we were able to develop experimental validation of the aerodynamic properties of the Samarai vehicle, with flight data calibrating our analytical models. We were also able to validate the basic approach for vehicle control that was developed based on these models. This effort clarified some of the challenges for sensors on a fully-rotating platform for sensing state of the vehicle and of the environment. We were able to make progress in addressing these challenges but more work remains in this area.

Having demonstrated the technical feasibility of the Samarai as a working air vehicle we are continuing this work with the twin objectives of more completely addressing the sensing challenges identified during the Samarai DAV prototyping effort described in this paper, and of more fully exploring the many benefits of the Samarai form laid out in the introduction. We are doing this through a new prototype (Figure 20), dubbed the Super Scale Prototype (SSP) for the fact that it is still larger than the objective 10 cm vehicle originally envisioned in [2].

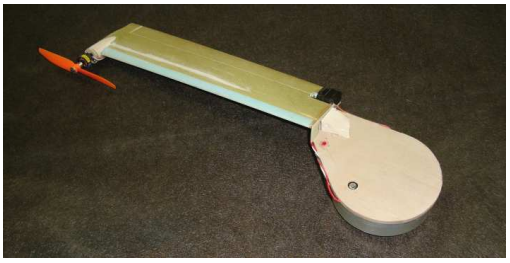

Figure 20. The current Samarai Super Scale Prototype (SSP) features a propulsion system mounted at the tip.

This vehicle is substantially smaller than the DAV, having a wing span of 30 cm with a target takeoff weight of 150 g. This design uses a propeller located at the tip of the wing to increase propulsion efficiency, and does not use a vertical stabilizer. At the time of this writing we have begun work with the SSP and expect future work to demonstrate a robust flight capability which can be used to execute operationally useful missions. Based on results shown to date, we believe that Samarai has a strong future as a multi-purpose, highly usable unique air vehicle.

ACKNOWLEDGMENTS

We would like to acknowledge Russ Frew and Chris Kubasik of Lockheed Martin for their sponsorship and support of this work. We would like to acknowledge the hard work, innovation, and dedication of all members of the Samarai team, including Ming Chang of Lockheed Martin Advanced Development Programs, and Dr. Bill Roberts and his team of North Carolina State University. We also thank Richard Perdichizzi and the MIT Aero & Astro Lab for use of their low-speed wind tunnel and instrumentation. Finally, we would like to acknowledge the vision of Dr. Ned Allen of Lockheed Martin Aeronautics, the originator of the Samarai concept.

REFERENCES

[1] The Delfly Micro, *Online documentation* available at: http://www.delfly.nl/?site=DIII&menu=home&lang=en (last accessed September 5th 2009)

[2] Youngren, H., Jameson, S., and Satterfield, B. "Design of the Samarai Monowing Rotorcraft Nano Air Vehicle," American Helicopter Society AHS 65th Annual Forum and Technology Display, Grapevine, TX, May 27-29, 2009.

[3] Ulrich, E., Pines, D., and Gerardi, S. "Autonomous Flight of a Samara MAV," American Helicopter Society AHS 65th Annual Forum and Technology Display, Grapevine, TX, May 27-29, 2009. *Online document available at: http://www.avl.umd.edu/projects/ulrich-files/Ulrich-AHS65.pdf* (last accessed Oct 29th 2009).

[4] "The Black Hornet," Prox Dynamics Inc, *Online documentation available at:* http://www.proxdynamics.com/news/prox_dynamics_hornet_3_prototype_is_flown_outdoors/ (last accessed September 5th 2009).

[5] Tournier, G., Valenti, M., How, J.P., and Feron, E. "Estimation and Control of a Quadrotor Vehicle Using Monocular Vision and Moire Patterns," 2006 AIAA Guidance, Navigation and Control Conference.

[6] Lentink, D. and Dickinson, M.H. "Biofluidynamic scaling of flapping, spinning and translating fins and wings," Journal of Experimental Biology, vol 16, July 31, 2009.

[7] Rosen, A. and Seter, D. "Vertical Autorotation of a Single-Winged Samara," ASME Joint Applied Mechanics/Bioengineering Conference, Ohio State University, Columbus, OH, June 16-19, 1991.

[8] Hoburg, W. "Fly-by-wire Control of a Monocopter," Technical Report, MIT, 2007. Online document available at: *http://rimworld.com/pgh/documents/hoburgmcreport.pdf* (last accessed Oct 29th 2009).

[9] Bakula, M., Hockley, C., Khatri, R., Kirby, C., Sammet, C., and Reinholtz, C. "A Natural Evolution in Flight: The Design and Development of the SamarEye System, A Method for Searching Closed Quarter Environments," 2009 AUVSI International Aerial Robotics Competition. *Online document available at: http://iarc.angel-strike.com/2009SymposiumPapers/2009EmbryRiddle.pdf* (last accessed Oct 29th 2009).

[10] Graham, F. *Monocopters*, Perigree Press, East Liverpool, OH, 1999.

[11] McCutchen, C.W. "Charles McCutchen's Flying Machines," *Aeromodeller*, vol. 19, (222), p. 350 ff. 1954.

[12] Leishman, J.G., "Principles of Helicopter Aerodynamics," 2000.

[13] Filippone, "Flight Performance of Fixed- and Rotary-Wing Aircraft," 2006.